Measurements of ^{59}Co$(d, p)^{60m,g}$Co, ^{51}V$(d, p)^{52}$V, and ^{nat}V$(d, xn)^{51}$Cr cross sections in the 2.7–5.4-MeV energy range

A. Kreisel,[1] L. Weissman,[1,*] A. Cohen,[1] T. Hirsh,[1] A. Shor,[1] O. Aviv,[1] I. Eliyahu,[1] M. Avrigeanu,[2] and V. Avrigeanu[2]

[1]*SARAF, Soreq Nuclear Research Center, 81800 Yavne, Israel*

[2]*Horia Hulubei National Institute for Physics and Nuclear Engineering, P.O. Box MG-6, 077125 Bucharest-Magurele, Romania*

(Received 12 October 2018; revised manuscript received 20 December 2018; published 19 March 2019)

The cross sections of the ^{59}Co$(d, p)^{60m,g}$Co, ^{51}V$(d, p)^{52}$V, and ^{nat}V$(d, xn)^{51}$Cr reactions were accurately measured at the Soreq Applied Research Accelerator Facility in the energy range 2.7–5.4 MeV. The obtained results together with other data, available in the same region of the nuclear chart, were used for verifying the theoretical models. The consistent theoretical model calculation successfully reproduces the experimental results.

DOI: 10.1103/PhysRevC.99.034611

I. INTRODUCTION

The present knowledge on deuteron induced nuclear cross sections is not sufficient and requires improvement. This demand is driven by two main factors.

First, introduction of a new generation of high-current deuteron accelerators [1] requires satisfactory accuracy in evaluation of activation of the accelerator components. This is especially critical because of demands for hands-on maintenance. In this context, the experimental data in the energy range of a few MeV are of special importance as the highest beam loss occurs at the first acceleration stages.

Furthermore, the lack of experimental data significantly limits the reliability and validity of the theoretical models of deuteron reaction processes and tabulated cross sections as found, for example, in the TALYS evaluations [2,3]. Predictions of these models and tabulated libraries can be validated only by reliable experimental data if available. For instance, reaction cross sections recommended most recently for the high-priority elements are still based on data fit, e.g., by various-order Padé approximations [4], with very low predictive power and disconnected from advances in nuclear modeling.

Second, the deuteron induced cross-section data at low beam energy, e.g., a few MeV, are of special theoretical interest due to the importance of the deuteron direct interactions and the associated phenomena. Most of the data available at low deuteron energy have large uncertainties. Since a deuteron beam of low energy is usually unavailable in research cyclotrons, standard foil stack techniques are used to measure cross sections with cyclotrons beams when it is desired to cover the broad energy range. However, passage of deuterons through multiple target foils results in a large energy straggling which leads to increasing uncertainties and reduced reliability of the cross-section results in the energy range of a few MeV. On the other hand, Van de Graaff dc accelerators cover the low-energy range and are characterized by a good ion energy definition; however, typical dc accelerator laboratories do not run deuterons due to lack of radiation safety measures and shielding.

Phase I of the Soreq Applied Research Accelerator Facility (SARAF) has been operational at Soreq Nuclear Research Center (NRC) [5] since 2008, while phase II of the project (deuteron energy up to 40 MeV) is under construction. The accelerating components of SARAF phase I consist of a four-rod radio-frequency quadrupole (RFQ) injector and a prototype superconducting module (PSM), which includes six half-wave resonator (HWR) superconducting cavities. Under normal operation parameters, the deuteron beam energy at phase I can be varied from 3 MeV (RFQ only) up to 5.5 MeV (RFQ and the HWR cavities). The deuteron beam energy spread is typically below 25 keV (sigma). Thus, SARAF phase I provides a unique beam energy range, which allows one to perform accurate cross-section measurements complimentary to the research performed at cyclotrons [6,7].

In this paper we combined the precise cross-section measurements in the unique SARAF phase I niche with thorough and consistent theoretical model calculations. Cobalt and vanadium targets were chosen for this showcase due to their importance as components of structural materials and accelerator technology (e.g., dosimetry and shielding), as well as in medical research (e.g., [8]). These targets were also chosen since both elements are metals having, essentially, only one natural isotope, ^{59}Co (abundance of 100%) and ^{51}V (abundance of 99.75%), thereby reducing the number of possible reaction channels. Thus, the analysis of the experimental results is straightforward and both cases can serve as an excellent benchmark for validation of the advanced theoretical models. In the case of cobalt, both the most recent [8] and the contradictory earlier cross-section measurements [9,10] were performed using the foil stack technique, while the ^{51}V$(d, p)^{52}$V cross section is measured for the first time in this paper.

*Corresponding author: weissman@soreq.gov.il

TABLE I. Reaction channels measured in this paper and γ rays (from [13,14]) used in the activation measurements.

Target	Abundance (%)	Channel	Threshold (MeV)	Product	Half-life	γ (keV)	Branching (%)
^{59}Co	100	(*d*,*p*)	0	^{60m}Co	10.467(6)min	58.6	2.07(3)
^{59}Co	100	(*d*,*p*)	0	^{60g}Co	1925.28(14)d	1173.2	99.85
						1332.5	99.98
^{51}V	99.75	(*d*,*p*)	0	^{52}V	3.743(5)min	1434.1	100.0
^{51}V	99.75	(*d*,2*n*)	3.098	^{51}Cr	27.702(1)d	320.1	9.91(1)
^{50}V	0.25	(*d*,*n*)	0	^{51}Cr	27.702(1)d	320.1	9.91(1)

II. EXPERIMENT

A. Targets

Cobalt and vanadium foils were ordered from Lebow, Inc. [11]. The 0.5-μm-thick cobalt layers were evaporated on 12-μm-thick 20 × 20-cm Kapton sheets. The individual targets were cut from the sheets and stretched on stainless steel ring frames. Pure metal vanadium targets on separate frames were ordered from the same company. These metallic foils were much thicker, nominally at 3.5 μm.

The thicknesses of the cobalt and vanadium targets used in the irradiations were measured using the Rutherford backscattering (RBS) method with 3-MeV He^+ ions. The RBS measurements were performed at the Ion Beam Analysis Laboratory, the Institute for Nanotechnology, Bar-Ilan University [12]. The measured thicknesses of the cobalt targets were in the range of 0.35-0.48 μm and the vanadium target thicknesses were in the range of 3.0-3.5 μm. A few 0.25-μm copper foils evaporated on 12.5-μm Mylar foils were used for beam energy verification (see below). The thickness of the copper targets was also measured by the same technique. The local thickness inhomogeneity of each target was found to be less than 3%, which was used as the experimental uncertainty. The RBS analysis method allows one to determine the target thickness directly in units of atoms per area, which is what is used in the cross-section calculation. The volume density of the target was not needed for the calculations.

The cobalt and vanadium targets were irradiated in the SARAF accelerator and later measured for radioactivity using a high-purity germanium (HPGe) detector. The properties of the target and reaction products are summarized in Table I. The reaction product associated with the low-abundant ^{50}V isotope is also included in the table. The experiment does not allow one to distinguish between the $^{51}V(d,2n)^{51}Cr$ and $^{50}V(d,n)^{51}Cr$ channels, although the contribution of the latter is significant only at the lowest energies. For consistency, the final results are quoted for the $^{nat}V(d,xn)^{51}Cr$ reaction.

B. Irradiations

The targets foils were installed on a target ladder located upstream of the SARAF beam dump (Fig. 1). A collimator and a quartz viewer were also installed on the ladder. A linear motion manipulator enabled one to either irradiate one of three target holder positions or remove the holder completely from the beam line. The quartz viewer and the target foil were monitored during beam tune and irradiation using a standard CCD camera.

Irradiation of single targets was performed for each target at a specific beam energy, which required frequent

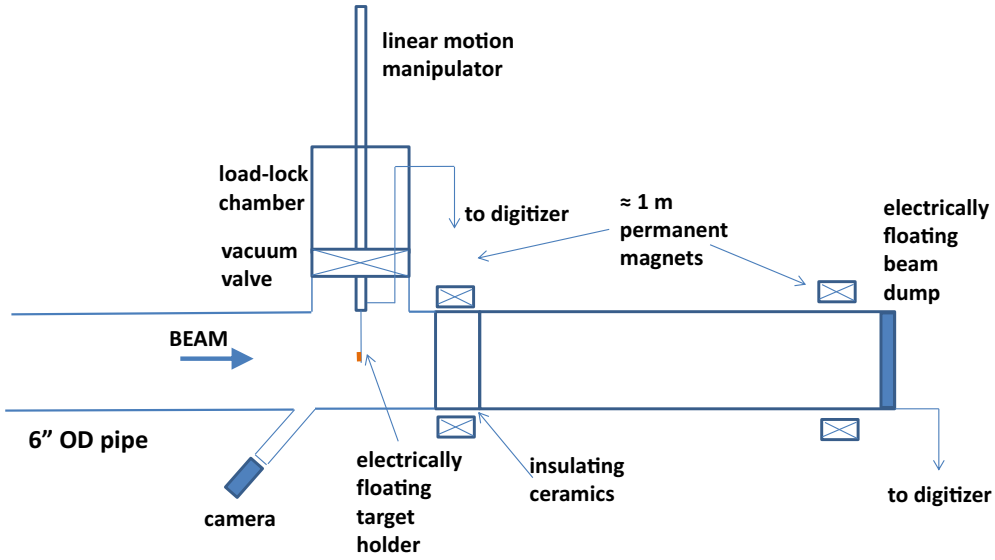

FIG. 1. A schematic view of the irradiation setup.

replacements of the targets without breaking the beam line vacuum. This was done using the load-lock chamber and a manual vacuum gate valve (Fig. 1). For the cobalt targets at each placement, it was verified that the evaporated cobalt side faced the beam. The Kapton backing of the thin cobalt foils ensured that all recoiling reaction products remained in the targets. Both the cobalt and vanadium foils were thin enough for the beam to pass through, even at the lowest beam energy tested. The beam current was measured on the electrically insulated beam dump, which was situated at a distance of 1.4 m downstream of the target holder (Fig. 1). A long beam pipe (≈1 m) adjacent to the dump and a set of strong permanent magnets ensured effective suppression of the secondary electrons (SEs). Further suppression of the SEs originating from the target holder was achieved using an additional set of strong permanent magnets that were mounted around the insulating ceramics. The target holder was also electrically insulated. Current collected on the target holder and the beam dump during irradiation was processed by digital current integrators (model ORTEC 439) and counted using scalars (model ORTEC 994) for accurate current integration. Prior to the experiment, the output accuracy of the current digitizers was checked with a high-precision calibration current source (model 263, Keithley). Current signal collected on the beam dump was digitized and recorded using an acquisition device (model NI9225, National Instrument). Typical beam current used during the irradiations was in the range of 200–300 nA, which was more than three orders of magnitude below the deuteron currents available at SARAF. A background current signal of 15–20 nA was observed on the beam dump. This signal was originated from the residual electric conductivity of the beam dump deionized cooling water. The background current was taken into account while determining the collected beam charge integrals. Typical irradiation periods were 10–30 min, depending on targets and beam energy.

The beam tune procedure prior to target irradiation was repeated for each specific energy and consisted of the following steps: (i) initial positioning of the beam on the quartz viewer, (ii) introduction of the collimator, and (iii) minimization and maximization of the currents on the collimator and beam dump, respectively. The same dimension (7 mm) of the collimator hole and the target foil ensured good beam tune prior to insertion of the foil.

Seven deuteron energies from 2.7 to 5.4 MeV were used for irradiations. The first PSM cavity was not used for acceleration but for beam bunching. For the highest energy all five subsequent cavities were used for acceleration at the highest possible fields. In order to obtain the lower beam energies, the voltages of the downstream cavities were reduced and they were gradually switched off. The lowest deuteron energy of 2.7 MeV was obtained by decelerating the 3-MeV beam exiting the RFQ using the second cavity.

The beam energy was measured using deuterons RBS from a thin gold foil [6]. This measurement was performed at the SARAF diagnostic plate placed 6.5 m upstream from the irradiation station. At a certain moment during these measurements it appeared that the gold foil had been damaged, which could result in a higher beam loss in the foil and higher uncertainty in determination of the beam energy. To validate the beam energy measurements, two copper foils were irradiated at the nominal energies of 5.4 and 4.3 MeV. The foils were used to measure the ^{63}Cu(d, p)^{64}Cu cross-section values and compare them with the previous accurate measurements [6]. As it is seen from the comparison (Fig. 2), there was indeed some inconsistency between the new and old results. In order to accommodate this experimental problem, the uncertainty in the beam energy was increased to 150 keV from the much lower conservative 50-keV value, which was previously quoted for the SARAF cross-section measurements [6,7].

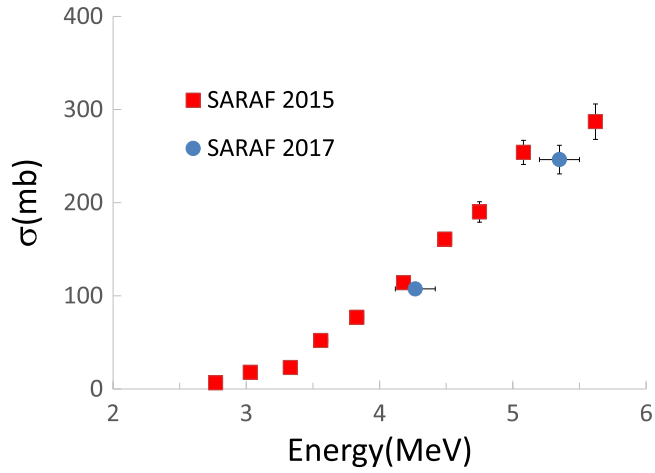

FIG. 2. Measured cross section of the ^{63}Cu(d, p)^{64}Cu reaction compared to the results of the previous experiment performed at similar conditions [6].

C. Radioactivity measurements

At the end of each irradiation, a target foil was quickly transported for activity measurements to a nearby shielded HPGe detector of 25% relative efficiency. The load-lock chamber (Fig. 1), used for quick extraction of targets, and the short distance (≈100 m) between the irradiation point and the HPGe detector allowed us to perform the challenging measurement of the ^{52}V and ^{60m}Co activities with short half-lives of 3.74 and 10.5 min, respectively. Each sample was measured twice: immediately after the irradiation and within one to two months after the irradiation due to very different half-lives of the reaction products (Table I). The clock of the computer recording the deuteron beam current on targets and that of the HPGe detector were synchronized with 1-s uncertainty. The detection of two short-lived isotopes ^{52}V and ^{60m}Co was further validated by analyzing their corresponding γ-ray peak count rate as a function of the elapsed time after irradiation. The time-dependent trend of the activities exhibited excellent agreement with the expected half-lives.

Examples of the γ spectra of irradiated samples are presented in Fig. 3.

The main contaminant γ rays in the spectra, 846 and 1810 keV, were associated with decay of ^{56}Mn($T_{1/2} = 2.58$ h). These γ rays are not seen in the spectra presented in Fig. 3 due to the different timing scale of the nuclei of interest. It became evident that the contaminants were produced on the stainless steel target frames via the ^{55}Mn(d, p)^{56}Mn reaction.

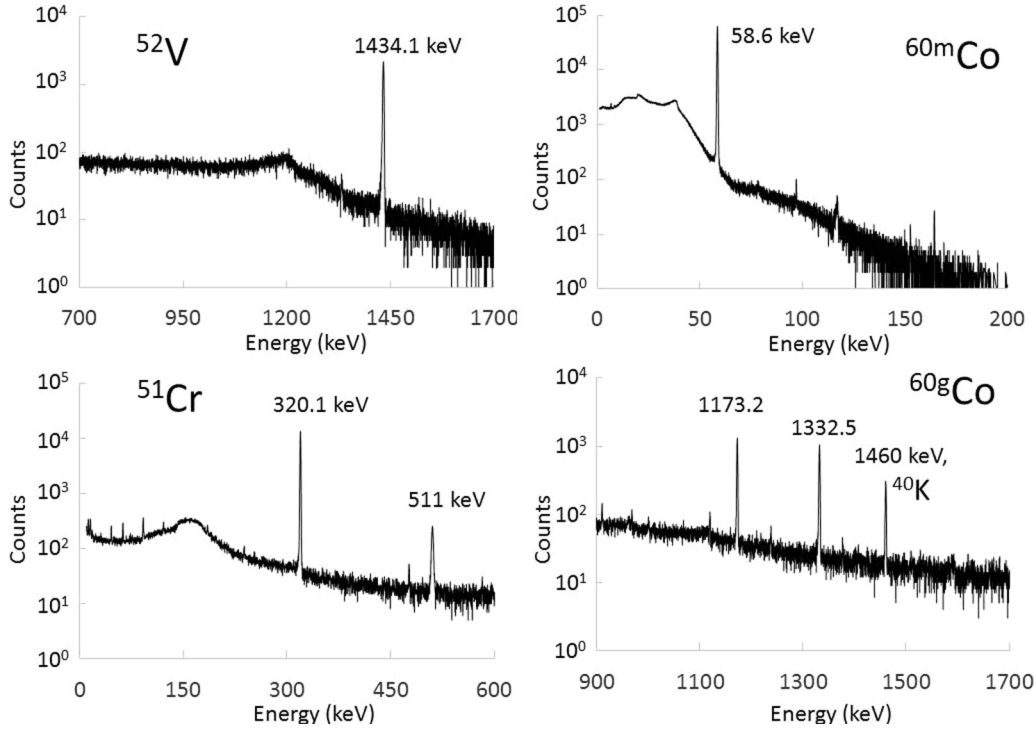

FIG. 3. Examples for the measured γ-ray spectra of the irradiated samples.

In a different measurement where the targets were separated from their frames, the contaminant γ rays were not observed in the spectra. Furthermore, the intensities of the γ-ray peaks originating from the activation products (Table I) were not affected by removing the steel frames, indicating that the whole activity of interest originated only from the target foils.

D. Results

The cross sections were determined from the measured activities of ^{52}V, ^{51}Cr, and ^{60m,g}Co, taking into account the decay losses during the irradiation, the detection efficiency, the branching ratios, the measurement duration (i.e., lifetime), the target thickness, the time-dependent beam current during irradiation, and the time lapse between the irradiations until start of the measurements. The contributions to the uncertainty of the cross section include the photopeak counts (0.6–20%), target thickness (3%), γ detection efficiency (1.4–4.6%), γ counting dead time estimation (less than 0.2%), deuteron beam current integral (2.1–4.7%), uncertainty in synchronization of the accelerator and Ge detector data acquisition clocks (<0.2%), and known uncertainties in the decay branching ratios. The total uncertainties in the cross-section values were deduced from adding the squares of these relative uncertainties.

The cross-section results for cobalt and vanadium are presented in Tables II and III, respectively. Determination of the ^{59}Co$(d, p)^{60g,m}$Co cross section, σ_g and $\sigma_{m,}$, requires special consideration. The σ_m cross section was measured immediately after irradiation, while the sum, $\sigma_g + \sigma_m$, was measured two months after the irradiation when all isomer nuclei decayed to the ground state (Table II). The measurement of ^{51}Cr activity is performed down to 3 MeV (Table III), which is lower than the threshold of the ^{51}V$(d, 2n)^{51}$Cr reaction. It is evident that the contribution of ^{50}V$(d, n)^{51}$Cr is not negligible in this energy range.

III. NUCLEAR MODEL ANALYSIS

Deuteron interactions at incident energies below and around the Coulomb barrier occur largely through direct reaction (DR) mechanisms of stripping and pick-up, while the preequilibrium emission (PE) and evaporation from the compound nucleoid (CN) become important with the increase of the incident energy. In addition, the specific deuteron breakup (BU) process plays an important role that increases the complexity of the deuteron interaction analysis in the incident-energy range of interest due to the variety of reactions initiated by the BU nucleons.

The simultaneous analysis of the deuteron elastic scattering and induced activation is a main constraint for consistent

TABLE II. Results for the ^{59}Co$(d, p)^{60g,m}$Co cross-section measurement.

Beam energy (MeV)	σ_m (mb)	$\sigma_m + \sigma_g$ (mb)	$\sigma_m/(\sigma_m + \sigma_{g_)}$
3.4(0.15)	30(6)	50(3)	0.60(13)
3.8(0.15)	32(6)	94(5)	0.34(7)
4.3(0.15)	56(5)	153(7)	0.37(4)
4.8(0.15)	93(9)	211(13)	0.44(5)
5.4(0.15)	122(6)	263(14)	0.46(3)

TABLE III. Results for the ^{51}V$(d, p)^{52}$V and ^{nat}V$(d, xn)^{51}$Cr cross sections.

Beam energy (MeV)	$\sigma[^{51}V(d, p)^{52}V]$ (mb)	$\sigma[^{nat}V(d, xn)^{51}Cr]$ (mb)
2.7(0.15)	19(1)	
3.0(0.15)	34(1.5)	0.13(1)
3.4(0.15)	60(2.5)	0.23(2)
3.8(0.15)	85(4)	0.36(5)
4.3(0.15)	172(6)	3.4(2)
4.8(0.15)	219(11)	25(2)
5.4(0.15)	286(14)	84(4.5)

nuclear model calculations and for a possible broad description of deuteron induced cross sections for the target nuclei and incident-energy range under consideration (e.g., [16–20]). Since details concerning the deuteron breakup and DR were given recently [[20] and references therein], only specific processes and parameter values are highlighted in the following. These include the distinct processes of elastic breakup (EB), in which the target nucleus remains in its ground state and none of the deuteron constituents interacts with it, and the inelastic breakup or breakup fusion (BF), where one of these deuteron constituents interacts inelastically with the target nucleus. The empirical parametrization [20] of EB and BF including total BU proton emission has been employed in the present paper. Otherwise, the DR contribution has been considered by means of the distorted-wave Born approximation (DWBA) method as shown below.

A. Deuteron optical potential

A primary interest in the optical model potential (OMP) is motivated by the further use of analysis of all deuteron interaction cross sections. However, the existence of only one measurement for deuteron elastic-scattering angular distribution for ^{50}V [21] as well as ^{59}Co [22] target nuclei at the low energies of interest for the present analysis hampers extended OMP analysis. Therefore, the predictions given by Lohr and Haeberli [23], Perey and Perey [24], Daehnick *et al.* [25], and An and Cai [26] for the global optical potentials for ^{50}V are shown in comparison with the experimental data at 7.5 MeV [21] in Fig. 4(a), with the best description corresponding to [23]. A similar comparison for 6.5-MeV deuterons elastically scattered on the ^{59}Co target nucleus [22] is shown in Fig. 4(b). Here it can be observed that the data are not well described by the above-mentioned potentials recommended for deuteron low energies. However, the data are described satisfactorily by the local OMP reported by Uehara [22].

B. Deuteron breakup contribution

The dominant BF component emphasizes the two opposite effects of the deuteron BU on the deuteron activation cross sections. Thus, the total-reaction cross section, σ_R, that is shared among different outgoing channels, is first decreased by the amount of the total BU neutron- and proton-emission cross section, σ_{BU}, shown in Fig. 5 for deuterons on ^{50,51}V and ^{59}Co target nuclei. Then, the BF component may bring significant contributions to various reaction channels [20,27]. So, the absorbed proton or neutron following the deuteron breakup contributes to the enhancement of the corresponding (*d,xn*) or (*d,xp*) activation cross sections, respectively. The assessment of the BF enhancement has been detailed previously ([20] and references therein) while the corresponding role of the BU nucleons during the deuteron interaction with ^{50,51}V and ^{59}Co through the (n, γ), (n, p), and (p, n) reactions is proved in the next section.

C. Direct reactions

The stripping, (*d,p*) and (*d,n*), and the pick-up, (*d,t*) and (d, a), DR are quite important for the first chance emitted particle process (e.g., [27–30]). The assessment of the total DR cross section is mandatory in deuteron activation analysis. Thus, the related decrease of the deuteron incident flux, in a similar way to the BU one, provides the correct total cross section going towards statistical processes. However, the

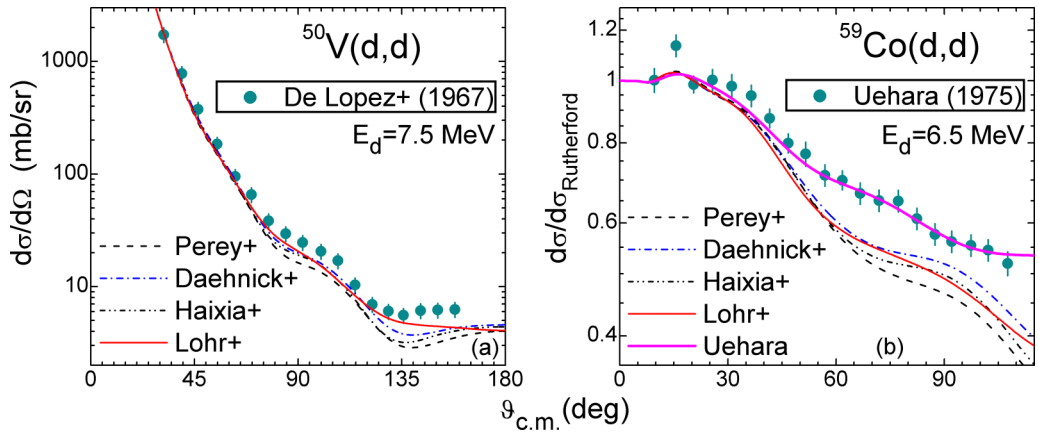

FIG. 4. Comparison of the measured [21,22] deuteron elastic-scattering angular distributions and results of calculations in this paper using the deuteron global OMP of Lohr and Haeberli [23] (thin solid curve), Perey and Perey [24] (dashed curve), Daehnick *et al.* [25] (dash-dotted curve), and An and Cai [26] (dash-dot-dotted curve) for (a) ^{50}V and (b) ^{59}Co target nuclei. The thick solid curve in panel (b) corresponds to Uehara [22] local OMP parameters.

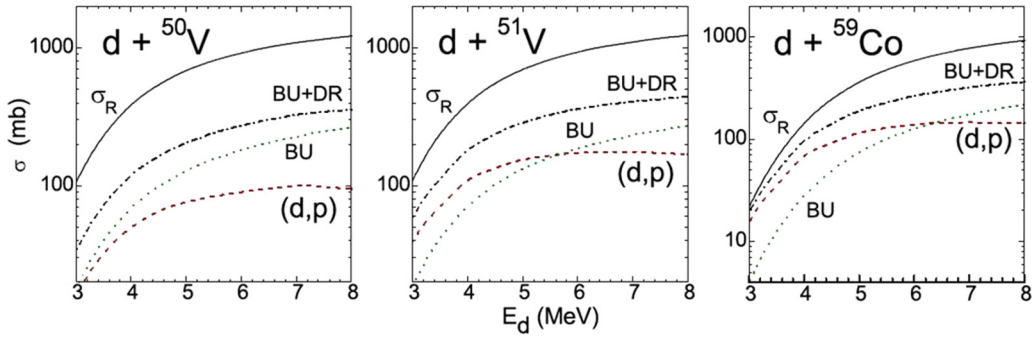

FIG. 5. Excitation functions calculated in this paper for total breakup (BU, dotted curves), direct (*d,p*) stripping (DR, dashed curves, see below), and total BU+DR direct interaction (dash-dotted curves) for deuteron interaction with ^{50,51}V and ^{59}Co target nuclei. The deuteron total-reaction cross sections (solid curves) correspond to the OMPs of Lohr and Haeberli [23] and Uehara [22], for $d+^{50,51}$V and $d+^{59}$Co interactions, respectively.

estimation of DR cross sections is constrained by the available experimental spectroscopic factors or at least by the outgoing particle angular distributions. While for the present analysis there are no data concerning the stripping (*d,n*) processes on ^{50,51}V and ^{59}Co target nuclei, we have obtained absolute values for the spectroscopic factors corresponding to the residual states populated in ^{52}V through the stripping ^{51}V$(d, p)^{52}$V process by normalization of the measured relative spectroscopic factors [31,32] to the theoretical values obtained from shell-model calculations by Gersch *et al.* [33].

The stripping (*d,p*) excitation functions for ^{50,51}V and ^{59}Co target nuclei have been calculated using the DWBA method within the FRESCO code [34]. The postform distorted-wave transition amplitudes and the finite-range interaction have been considered. The (*n,p*) effective interaction in deuteron [35] has been assumed, while the transferred nucleon bound states were generated in a Woods-Saxon real potential [20,27]. The spectroscopic information which has been available within the ENSDF library [11,13,36] and experimental works of [21,22,31,32] was used. The population of 50 discrete levels up to the excitation energy of 6.56 MeV in ^{51}V [13] and that of 33 discrete levels up to the excitation energy of 3.66 MeV in ^{52}V [12] residual nuclei have been considered, while for the ^{60}Co residual nucleus the stripping cross-section calculations involved 119 discrete levels up to 6 MeV [11]. However, since the DR population of higher states continues, even with lower weighting [37,38], a correction has been applied for the target nucleus ^{59}Co on the basis of the calculated DR reaction cross-section dependence on the residual-nucleus excitation energy. Thus, beyond an obvious maximum of this dependence, the decrease for lower DR emitted particle energies has been extended up to the Coulomb barrier. An increase from 15 to 39% of the stripping (*d,p*) reaction cross section has consequently been obtained for the deuteron incident energies from 3 to 6 MeV. A comparison of the experimental [21,22,31] and calculated angular distributions of the stripped protons from the (*d,p*) transfer reactions on ^{50}V and ^{59}Co target nuclei is shown in Fig. 6. The description of the measured data validates the calculated total stripping cross sections shown in Fig. 5. However, the sum of the total BU and stripping (*d,p*) cross sections gives only a lower limit for the contribution of direct interactions (DIs), i.e., DI = BU + DR, to the deuteron interaction with ^{50,51}V and ^{59}Co target nuclei, as long as the (*d,n*) stripping contribution is missing due to the lack of any experimental data. On the other hand, the pick-up processes are very weak at the low energies of interest for the present analysis, namely, under the Coulomb barrier for (*d,α*) reactions, and around the threshold for the (*d,t*) ones. Very scarce related spectroscopic information should be also noted.

D. Statistical emission

Subsequent to the DI analysis, the deuteron OMP total-reaction cross section was corrected by subtraction of the BU+DR cross sections and then used for PE+CN statistical emission. An updated version of the code STAPRE-H [39] was used for this analysis. Values of ∼0.2− and 0.3-MeV equidistant binning were used for the excitation energy grid for incident energies either below or above 10 MeV. We may add, for the sake of completeness, that the PE geometry-dependent hybrid model ([40] and references therein) has been used within the STAPRE-H code for nucleon and *a*-particle PE emission including angular momentum conservation and advanced partial level densities [41,42]. Moreover, a local consistent parameter set has been used, which was obtained or checked through the analysis of various independent experimental data, in advance of the deuteron cross-section analysis and is also involved within quite similar PE+CN analysis of neutron-induced reactions on V [43] and Co [44] isotopes. Nuclear-level density parameters which have been updated on the basis of the most recent information on the low-lying levels [36] and nucleon resonance data [45] have been of less importance for the results of the present paper. A particular note with reference to the analysis of the isomeric cross-section ratio of the ^{59}Co$(d, p)^{60m,g}$Co reaction may concern the use of the same level-density spin dependence proved suitable within a study of the same state population through neutron-induced reactions [44]. However, a particular analysis had to concern the proton OMP, in order to provide an increased accuracy to the calculated (*d,p*) reaction cross sections for the ^{60}Co target nucleus. While usually the analysis of the (*p,n*) reaction cross sections is most useful for the validation of the proton OMP, also the (p, γ) reaction cross-section analysis has a key importance below the (*p,n*) reaction threshold. Analysis of the

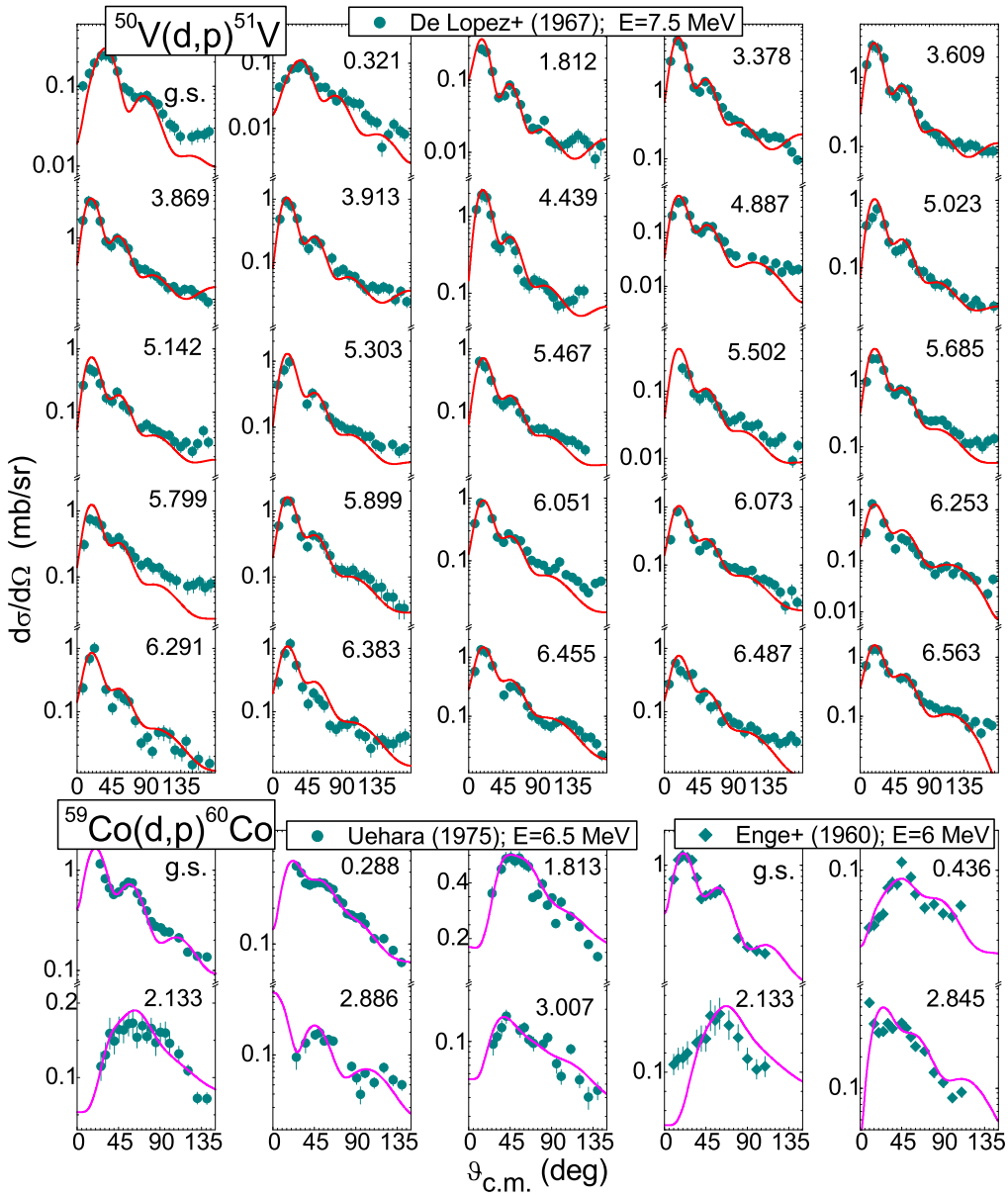

FIG. 6. Comparison of measured [21,22,31] and calculated in this paper (solid curves) proton angular distributions from the (d,p) transfer reactions on ^{50}V and ^{59}Co target nuclei at incident energies of 7.5 MeV and of 6.5 and 6.01 MeV, respectively, corresponding to the residual nucleus states shown in the figure.

experimental data on the ^{59}Co(p, n)^{59}Ni and ^{59}Co(p, g)^{60}Ni reactions allowed us to validate the proton OMP. Thus, it was found [44] that the widely used global proton OMP of Koning and Delaroche [46] led to either underestimation or overestimation of the measured (p, γ) and (p,n) reaction cross sections [47], respectively. Therefore, we have also used for the present analysis the local proton OMP of Hetrick *et al.* [48] as modified at lower energies, e.g. [49], with the good results shown in Fig. 2 of [44].

IV. DISCUSSION

The experimental results for the cross sections obtained for the reactions ^{51}V(d, p)^{52}V, $^{\rm nat}$V(d, xn)^{51}Cr, and ^{59}Co(d, p)$^{60(g+m)}$Co are shown in Figs. 7 and 8 together with results from previous works and theoretical models [8–10,50–55]. While there are no available earlier experimental data on the ^{51}V(d, p)^{52}V cross section, it is interesting to compare the present results for the $^{\rm nat}$V(d, xn)^{51}Cr and ^{59}Co(d, p)$^{60(g+m)}$Co cross sections to the previous experiments. The present data are of much better quality than results of the experiments performed with foil stack technique. The present data should therefore have much higher weight for testing of theoretical models.

The theoretical calculations presented in Figs. 7 and 8 include detailed contributions of various reaction mechanisms described above, as well as predictions of the TALYS-1.9 code [2] and TENDL-2017 library [3]. The default predictions of

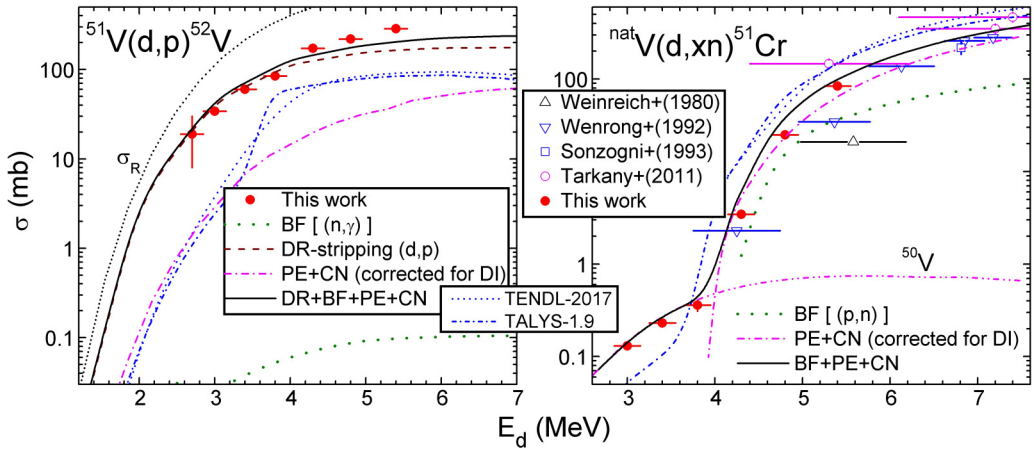

FIG. 7. Comparison of the experimental results for ^{51}V$(d, p)^{52}$V (left) and ^{nat}V$(d, xn)^{51}$Cr (right) cross sections with the theoretical calculations of this paper (Fig. 5). The main contributions of the calculated cross sections (solid curves) are stripping (*d,p*) reaction (dashed curves), BF enhancement (dash-dot-dotted curves), and PE + CN (dash-dotted curves) components, including the contribution of the ^{50}V$(d, n)^{51}$Cr reaction (dash-dot-dotted curve), corrected for DI deuteron flux leakage. The TENDL-2017 [3] evaluation (short-dashed curves) and calculation results of this paper using the code TALYS-1.9 [2] and its default parameters (short dash-dotted curves) are shown. The earlier experimental data [50–53] available for ^{nat}V$(d, xn)^{51}$Cr as well as the deuteron total-reaction cross section [23] for the ^{51}V target nucleus (short dotted curve) are also presented.

TALYS-1.9 were used in order to do a comparison of the results of this paper with a global approach. The BU processes are taken into account in TALYS through the addition of the Kalbach's parametrization of the total BU cross section [56] to the usual PE excitation model results ([57] and references therein). The content of the evaluated data library TENDL-2017 [3], which is based on particularly adjusted TALYS calculations in order to describe the measured data, has been used in the same respect.

Data available at similar lower energies for the reaction ^{59}Co$(d, 2p)^{59}$Fe [8,54,55] have been also compared with the theoretical predictions (Fig. 8) in order to prove the consistent modeling of all data available for a target nucleus within the same incident-energy range. All the theoretical calculation parameters were chosen and adjusted using experimental information available in the literature (previous section). No additional parameter tune was done in order to obtain the calculated results shown in Figs. 7 and 8.

The proper implementation of the reaction mechanisms that have been considered in the present paper is demonstrated by the overall agreement of the experimental and calculated excitation functions. The calculated cross-section results are much more successful than the results of TALYS and TENDL, even with the best possible adjustment of the default

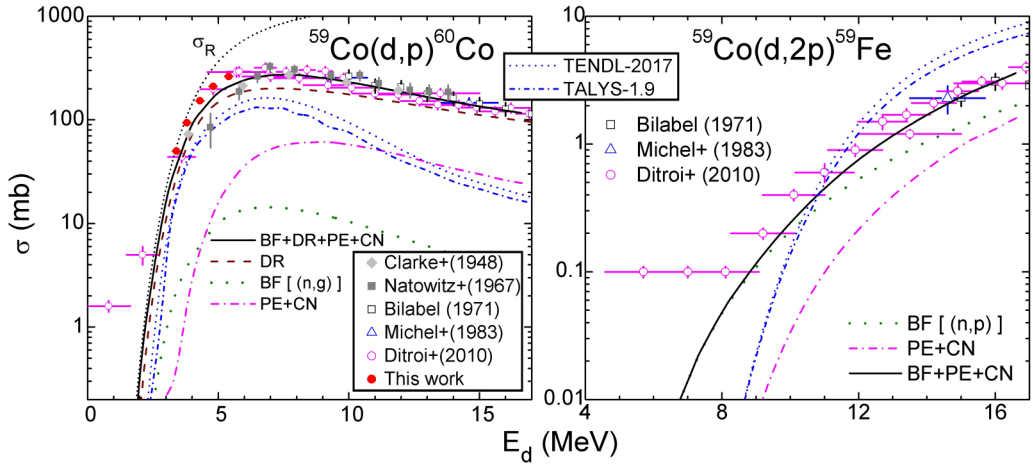

FIG. 8. Comparison of previous [8–10,14,15] and present (solid circles) measurements of (*d,p*) and (*d,2p*) reaction cross sections for the ^{59}Co target nucleus, TENDL-2017 [3] evaluation (short-dashed curves), and calculation results of this paper using the code TALYS-1.9 [2] and its default parameters (short dash-dotted curves), as well as of the present paper (solid curves), along with stripping (*d,p*) reaction (dashed curves), BF enhancement (dash-dot-dotted curves), and PE+CN (dash-dotted curves) components corrected for DI deuteron flux leakage.

parameters of the later codes. Additionally, particular note should be made concerning the theoretical account of the direct stripping (*d,p*) reaction cross sections. The lower agreement at higher incident energies on the target nucleus ^{51}V (Fig. 7), as well as the need for the above-described DR correction, proved necessary for the target nucleus ^{59}Co. Figure 8 may point out the usefulness of a more suitable consideration of the stripping (*d,p*) reaction in the continuum of the excited residual nucleus [37,38].

On the other hand, related model questions are pointed out especially by measurements at the low energies of the present paper. Their significant value is particularly shown in the case of the deuterons incident on the ^{59}Co target nucleus at energies below 5 MeV, where the present measurements and analysis support the more recent data [8] and the former one [10], at variance with the more than twice lower earlier data [9] and latest evaluations [2,3].

V. SUMMARY

The cross sections of the ^{59}Co$(d, p)^{60m,g}$Co, ^{51}V$(d, p)^{52}$V, and ^{nat}V$(d, xn)^{51}$Cr reactions were accurately measured at the SARAF linear accelerator facility in the energy range 2.7–5.4 MeV. The high-quality cross-section measurements obtained with monoisotopic targets present an excellent opportunity for testing theoretical calculations in the low-energy region, sensitive to the different reaction mechanisms contributing to the activation cross section.

Concerning the nuclear model analysis of the deuteron induced reactions within this paper, first it should be mentioned that the deuteron OMPs of Lohr and Haeberli [23] and Uehara [22] have been employed for the vanadium and cobalt target nuclei, respectively, on the basis of the available elastic-scattering data analysis. Then, with the BU and BF analysis methods described earlier ([20,27] and references therein), calculation of the DR stripping cross sections has been expanded up to 50, 33, and 119 excited states with known angular distributions in ^{51,52}V and ^{60}Co nuclei, respectively. Moreover, the PE+CN analysis has been carried out with the STAPRE-H code [39] using, in particular, local parameters carefully checked in advance. The rather important proton OMP developed earlier by Hetrick *et al.* [48], as modified at lower energies in [49], has additionally been adopted.

The calculations agree with the present experimental results to a much better extent than those of the broadly used TALYS code [2] and the corresponding evaluations [3]. At the same time, the present paper proves, also for reactions well below the Coulomb barrier, the benefit of the consistent model calculations, while the recently recommended reaction cross sections for high-priority elements on the basis of data fit [4] are characterized by low predictive power and disconnected from advances in nuclear modeling. The obtained results on the isomeric production ^{59}Co$(d, p)^{60m,g}$Co ratio (Table II) call for further experimental investigation.

ACKNOWLEDGMENTS

We are grateful to Dr. O. Girshevitz from Bar-Ilan University for her measurement of the target foil thicknesses. We are thankful to the SARAF team for running the accelerator. This work has been partly supported by Autoritatea Nationala pentru Cercetare Stiintifica (PN-18090102), Romania. The authors are grateful to Dr. D. Berkovits for his comments on the paper.

[1] J.-L. Biarrotte, MOIOB01, SRF2013, Paris, France, 2013, http://www.jacow.org.
[2] A. J. Koning, S. Hilaire, M. C. Duijvestijn, ND2007, EDP Sciences, Nice, France, 2008, pp. 211–214, http://www.talys.eu.
[3] A. J. Koning, D. Rochman, TENDL-2017: TALYS-based evaluated nuclear data library, https://tendl.web.psi.ch/tendl_2017/tendl2017.html (30 December 2017).
[4] A. Hermanne *et al.*, Nucl. Data Sheets **148**, 338 (2018)
[5] I. Mardor *et al.*, Eur. Phys. J. A **54**, 91 (2018).
[6] L. Weissman, A. Kreisel, T. Hirsh, O. Aviv, D. Berkovits, O. Girshevitz and Y. Eisen., Nucl. Instrum. Methods B **342**, 7 (2015).
[7] T. Hirsh *et al.*, Nucl. Instrum. Methods B **362**, 29 (2015).
[8] F. Ditroi, F. Tarkanyi, S. Takacs, A. Hermanne, M. Baba, and A. V. Ignatyuk, Nucl. Instrum. Methods B **268**, 2571 (2010).
[9] J. B. Natowitz and R. L. Wolke, Phys. Rev. **155**, 1352 (1967).
[10] D. C. Peaslee, Phys. Rev. **74**, 1001 (1948).
[11] www.lebowcompany.com.
[12] www.nano.biu.ac.il.
[13] E. Browne and J. K. Tuli, Nucl. Data Sheets **114**, 1849 (2013).
[14] Y. Dong and H. Junde, Nucl. Data Sheets **128**, 185 (2015).
[15] J. Wang and X. Huang, Nucl. Data Sheets **144**, 1 (2017).
[16] S. Nakayama, H. Kouno, Y. Watanabe, O. Iwamoto, and K. Ogata, Phys. Rev. C **94**, 014618 (2016).
[17] M. Febbraro, F. D. Becchetti, R. O. Torres-Isea, J. Riggins, C. C. Lawrence, J. J. Kolata, and A. M. Howard, Phys. Rev. C **96**, 024613 (2017).
[18] A. Pakou *et al.*, Eur. Phys. J. A **53**, 167 (2017).
[19] S. Nakayama, N. Furutachi, O. Iwamoto, and Y. Watanabe, Phys. Rev. C **98**, 044606 (2018).
[20] M. Avrigeanu and V. Avrigeanu, Phys. Rev. C **95**, 024607 (2017).
[21] M. E. de Lopez, M. Mazari, T. A. Belote, W. E. Dorenbusch, and O. Hansen, Nucl. Phys. A **94**, 673 (1967).
[22] S. Uehara, J. Phys. Soc. Japan **38**, 936 (1975).
[23] J. M. Lohr and W. Haeberli, Nucl. Phys. A **232**, 381 (1974).
[24] C. M. Perey and F. G. Perey, Phys. Rev. **132**, 755 (1963).
[25] W. W. Daehnick, J. D. Childs, and Z. Vrcelj, Phys. Rev. C **21**, 2253 (1980).
[26] H. An and C. Cai, Phys. Rev. C **73**, 054605 (2006).
[27] M. Avrigeanu and V. Avrigeanu, Phys. Rev. C **92**, 021601 (2015).
[28] R. M. DelVecchio, Phys. Rev. C **7**, 677 (1973).
[29] G. Potel, F. M. Nunes, and I. J. Thompson, Phys. Rev. C **92**, 034611 (2015); A. Ross, L. J. Titus, and F. M. Nunes, *ibid.* **94**, 014607 (2016).

[30] G. Potel *et al.*, Eur. Phys. J. A **53**, 178 (2017).
[31] H. A. Enge, D. L. Jarrell, and C. C. Angleman, Phys. Rev. **119**, 735 (1960).
[32] J. Catala, A. Garca, J. M. Bolta, S. Hinds, H. Marchant, and A. E. Forest, Nucl. Phys. **74**, 1 (1965).
[33] H. U. Gersch, C. Riedel, and W. Rudolph, Nucl. Phys. A **97**, 65 (1967).
[34] I. J. Thompson, Comp. Phys. Rep. **7**, 167 (1988).
[35] Y. Iseri, M. Yahiro, and M. Kamimura, Prog. Theor. Phys. Suppl. **89**, 84 (1986).
[36] http://www.nndc.bnl.gov/ensdf/.
[37] J. Lei and A. M. Moro, Phys. Rev. C **92**, 044616 (2015).
[38] J. Lei and A. M. Moro, Phys. Rev. C **97**, 011601 (2018).
[39] M. Avrigeanu and V. Avrigeanu, Institute for Physics and Nuclear Engineering Report No. NP-86-1995, 1995 (unpublished), http://www.oecd-nea.org/tools/abstract/detail/iaea0971.
[40] M. Blann and H. K. Vonach, Phys. Rev. C **28**, 1475 (1983).
[41] M. Avrigeanu and V. Avrigeanu, Comp. Phys. Comm. **112**, 191 (1998).
[42] A. Harangozo, I. Ştefcu, M. Avrigeanu, and V. Avrigeanu, Phys. Rev. C **58**, 295 (1998).
[43] P. Reimer, V. Avrigeanu, A. J. M. Plompen, and S. M. Qaim, Phys. Rev. C **65**, 014604 (2001).
[44] V. Semkova, V. Avrigeanu, T. Glodariu, A. J. Koning, A. J. M. Plompen, D. L. Smith, and S. Sudar, Nucl. Phys. A **730**, 255 (2004).
[45] R. Capote *et al.*, Nucl. Data Sheets **110**, 3107 (2009).
[46] A. J. Koning and J. P. Delaroche, Nucl. Phys. A **713**, 231 (2003).
[47] http://www-nds.iaea.org/exfor/.
[48] D. M. Hetrick, C. Y. Fu, and D. C. Larson, Rad. Effects **95**, 191 (1986).
[49] M. Avrigeanu, S. V. Chuvaev, A. A. Filatenkov, R. A. Forrest, M. Herman, A. J. Koning, A. J. M. Plompen, F. L. Roman, and V. Avrigeanu, Nucl. Phys. A **806**, 15 (2008).
[50] A. A. Sonzogni, A. S. M. A. Romo, H. O. Mosca, and S. J. Nassiff, J. Rad. Nucl. Chem. **170**, 143 (1993).
[51] Z. Wenrong, L. Hanlin, and Y. Weixiang, Chinese J. Nucl. Phys. **14**, 309 (1992); EXFOR Data Entry No. S00390, dated 1994-06-24, https://www.nndc.bnl.gov/exfor/servlet/X4sGetSubent?reqx=85638&subID=280039002.
[52] R. Weinreich, H. J. Probst, and S. M. Qaim, Appl. Rad. Isot. **31**, 223 (1980).
[53] F. Tárkányi, F. Ditrói, S. Takács, A. Hermanne, M. Baba, and A. V. Ignatyuk, Nucl. Instrum. Methods B **269**, 1792 (2011).
[54] R. Michel and M. Galas, Appl. Rad. Isot. **34**, 1325 (1983).
[55] R. Bilabel, Radioch. Acta **15**, 13 (1971).
[56] C. Kalbach Walker, FENDL Technical Report, IAEA, 2010, http://www.nds.iaea.org/fendl3/vardocs.html.
[57] A. J. Koning and M. C. Duijvestijn, Nucl. Phys. A **744**, 15 (2004).